



# Planar Solid Oxide Fuel Cell Fabricated by Aqueous Reverse Sequential Tape-Casting of the Anode, Electrolyte, and Barrier Layer

Laura Parvaix, Sandrine Duluard, Florence Ansart, Pascal Lenormand,  
Patrick Rozier

## ► To cite this version:

Laura Parvaix, Sandrine Duluard, Florence Ansart, Pascal Lenormand, Patrick Rozier. Planar Solid Oxide Fuel Cell Fabricated by Aqueous Reverse Sequential Tape-Casting of the Anode, Electrolyte, and Barrier Layer. *Energy Technology*, 2023, 11 (10), 10.1002/ente.202300020 . hal-04276721

**HAL Id: hal-04276721**

**<https://hal.science/hal-04276721v1>**

Submitted on 9 Nov 2023

**HAL** is a multi-disciplinary open access archive for the deposit and dissemination of scientific research documents, whether they are published or not. The documents may come from teaching and research institutions in France or abroad, or from public or private research centers.

L'archive ouverte pluridisciplinaire **HAL**, est destinée au dépôt et à la diffusion de documents scientifiques de niveau recherche, publiés ou non, émanant des établissements d'enseignement et de recherche français ou étrangers, des laboratoires publics ou privés.



Distributed under a Creative Commons Attribution 4.0 International License

# Planar Solid Oxide Fuel Cell Fabricated by Aqueous Reverse Sequential Tape-Casting of the Anode, Electrolyte, and Barrier Layer

Laura Parvaix, Sandrine Duluard, Florence Ansart, Pascal Lenormand,\* and Patrick Rozier

A low-cost manufacturing procedure has been developed for the fabrication of planar anode-supported solid oxide fuel cell including only two thermal treatments. This method is also environmental friendly because slurries are water based and use nontoxic additives. Slurries are formulated by optimizing the powder quantity, by minimizing the organic compounds while controlling their stabilities and their rheological properties. Flexible multilayer green tapes have been produced by using the reverse sequential tape-casting method. After a cosintering thermal treatment under loads, planar anodic half-cells have been produced allowing the deposition of a  $\text{La}_2\text{NiO}_{4+\delta}$  cathode by screen printing. After the final consolidation thermal treatment, the cell presents a 30  $\mu\text{m}$ -thick porous cathode, a 530  $\mu\text{m}$ -thick NiO-YSZ porous anode, and a 80  $\mu\text{m}$ -thick dense electrolyte with a gradient of composition: 10GDC on the cathode side to prevent the apparition of the  $\text{La}_2\text{Zr}_2\text{O}_7$  insulating phase and 8YSZ on the anode side to avoid the reduction of 10GDC with the fuel gas. Power densities present promising performances (319  $\text{mW cm}^{-2}$  at 830  $^\circ\text{C}$ ) given that electrolyte thickness and electrochemical system measurement may be improved.

commercialization of SOFC is slowed down due to the still high manufacturing and material cost. For this reason, many recent studies have been made to find cost-effective production methods.<sup>[1]</sup>

To overcome the challenge of obtaining a dense layer of yttria-stabilized zirconia 8YSZ (electrolyte) on a porous cermet Ni-8YSZ anode, the commonly followed process consists of assembling a full oxide precursor of the SOFC, the NiO-8YSZ oxide precursor being selectively reduced during the warming up to generate in situ the anodic cermet.

In addition to the electrolyte and the anode, the all oxide half-cell includes ceria doped gadolinium (GDC) deposited by screen printing on top of the electrolyte and acting as a diffusion barrier layer (DBL) to avoid the formation of the  $\text{La}_2\text{Zr}_2\text{O}_7$  insulating phase at the cathode/electrolyte interface during the screen-printed


$\text{La}_2\text{NiO}_{4+\delta}$  (LNO) cathode consolidation thermal treatment.<sup>[2,3]</sup> The shaping of the different components of the oxide precursor of the full cell is made using the tape-casting process, a widely used technique at the industrial scale as compared to other processes such as chemical or physical vapor deposition. Besides being low cost and easily scalable, this process also allows controlling the microstructure (dense or porous) and thicknesses (from 5 to 1000  $\mu\text{m}$ ) of produced ceramic layers. The conventional approach consists in casting the anodic and electrolyte layers individually and assembling them in a second step consisting in lamination and hot-pressing process to form the anodic multilayer. In a third step, a diffusion barrier layer is classically sprayed or screen-printed before sintering. The fourth step consists in the deposition of the cathode layer by screen-printing and the full cell is obtained by a final consolidation thermal treatment.<sup>[4–6]</sup> Recently, to decrease the number of steps, the sequential tape-casting process of anode, electrolyte, and diffusion barrier layers has been successively proposed. In this process, slurries of anode and electrolyte are casted on top of each other with only a quick drying step between each casting and the stack is cosintered resulting in homogeneous layers and strong interfaces.<sup>[7–10]</sup>

Also, the nature of the slurries which are constituted of organic solvents (toluene, xylene, ethanol), toxic additives, and

## 1. Introduction

Hydrogen technologies and especially fuel cells are promising alternatives to achieve a carbon-free energy and an eco-friendly transition. The solid oxide fuel cell (SOFC) technology is an energy conversion system composed of a stack comprising a porous cathode, a dense electrolyte, and a porous anode inserted between metallic interconnects working at a temperature in the [600–1000  $^\circ\text{C}$ ] temperature range necessary to obtain ionic conductivity above  $10^{-2} \text{ S cm}^{-1}$  in the electrolyte. However, the

L. Parvaix, S. Duluard, F. Ansart, P. Lenormand, P. Rozier  
CIRIMAT  
Université de Toulouse, CNRS  
Université Toulouse 3 - Paul Sabatier  
118 Route de Narbonne, 31062 Toulouse cedex 9, France  
E-mail: pascal.lenormand@univ-tlse3.fr

 The ORCID identification number(s) for the author(s) of this article can be found under <https://doi.org/10.1002/ente.202300020>.

© 2023 The Authors. Energy Technology published by Wiley-VCH GmbH. This is an open access article under the terms of the Creative Commons Attribution License, which permits use, distribution and reproduction in any medium, provided the original work is properly cited.

DOI: 10.1002/ente.202300020

binders which increase the production cost, and the waste management as well as being harmful for human health and environment. To solve that, researches of nontoxic and aqueous-based slurries have been developed and show that, to counterbalance the polarity of water molecules, the use of acrylic latex commercial emulsion or polyvinyl alcohol (PVA) as binder allows optimizing slurry dispersion and stability.<sup>[11–15]</sup>

Following these principles, Snowden et al. successfully produced an anodic half-cell including the DBL layer by sequential tape-casting.<sup>[14]</sup> Slurries were composed of oxide powders of NiO-ScCeSZ for anode, ScCeSZ for electrolyte, and a 10GDC ( $\text{Ce}_{0.9}\text{Gd}_{0.1}\text{O}_2$ ) as diffusion barrier layer but only the anode slurry was aqueous with a PVA binder, the others were composed of commercial binder solutions which are expensive and with a nonadjustable composition.

To achieve low-cost and eco-friendly process for the whole manufacturing of the SOFC, this article reports the outcomes to produce in only two thermal treatment steps, anode-supported SOFC by reverse sequential tape-casting of the anodic half-cell including the DBL. The detailed study of the slurries formulation, the elimination of organics, and the cosintering process allowed reaching the final flat multilayer anodic half-cell with optimized microstructures and thicknesses. The cell was completed by screen printing of  $\text{La}_2\text{NiO}_{4+\delta}$  (cathode)-based ink followed by a consolidation thermal treatment. The characterizations using X-ray diffraction (XRD), scanning electron microscopy (SEM), and operando electrochemical tests of the cell allow validating both the concept of all oxide precursors and the efficiency of the sequential tape-casting process to fabricate eco-friendly and low-cost SOFC.

## 2. Results and Discussion

To allow the reverse sequential tape-casting of the different components of the full anodic half-cell while targeting eco-friendly process, the nature and amount of slurry components have to be selected to target, as main criteria, a stable dispersion with controlled viscosity and a shear thinning mechanical behavior. These criteria being also largely dependent on the loading of solid component to be shaped, the electrolyte slurry with the highest solid/solution ratio has been first optimized. The formulation and architecture of the whole stack have been detailed and shaped in a second step.

### 2.1. Electrolyte Slurry Optimization

Yttrium-stabilized zirconia (8YSZ) has been selected as the electrolyte material. The SEM images (Figure S1, Supporting Information) show that the morphology corresponds to spherical particles with a narrow monomodal distribution in the range of 30–100 nm with an average grain size of 65 nm as deduced from image analysis (Figure S2, Supporting Information).

Zeta potential measurements and sedimentation test were performed to find out the optimum amount of dispersant needed to stabilize the aqueous suspension of 8YSZ. The zirconia powder was dispersed in water with ammonium polymethacrylate (NH4PAA) which is a widely used polyelectrolyte surfactant.<sup>[9,16–19]</sup> This test was performed in a range of 1–4 wt% of dispersant to

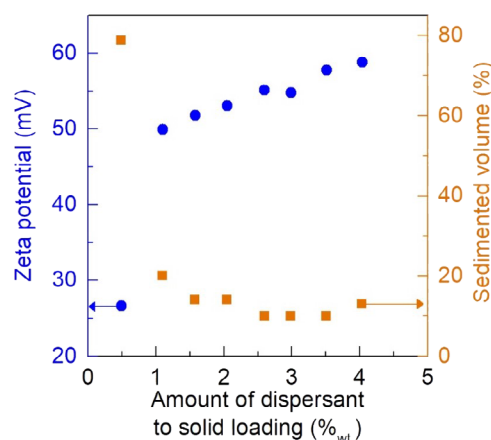


**Figure 1.** Zeta potential and sedimentation volume of an 8YSZ/water suspension as a function of ammonium polyacrylate dispersant amount.

solid loading which are typical values for zirconia aqueous dispersions.<sup>[17,20–26]</sup> As shown in **Figure 1**, a large increase of the zeta potential from 27 to 50 mV can be noticed with, respectively, 0.5 and 1 wt% of dispersant and is followed by a small evolution while increasing the dispersant content up to 4%. The sedimentation volume measured after 24 h drastically decreases from 55% to 14% with, respectively, 0.5 and 1 wt% of dispersant and stabilizes around a sediment volume of 10% with an increase of dispersant up to 4 wt%. The optimal amount of dispersant leading to highest zeta potential (58 mV) and the lowest sediment volume (10%) is determined to be 3.5 wt%. However, the actual gain in performances being low with the increase of the dispersant content above 1 wt%, and then 1 wt% dispersant to solid loading is selected to minimize the additive content of the slurry and maintain suitable properties (zeta potential 50 mV, sediment volume 30%).

A water-based suspension was then prepared by gradually adding the 8YSZ powder in water with the selected optimum amount of dispersant (1 wt% of dispersant to solid loading). Agglomerates were eliminated by using an ultrasonic bath during 10 min. Then, the dispersion was mixed in a planetary centrifugal mixer at 1000 rpm during 7 min and at 2000 rpm during 2 min.

PVA is selected as a binder and PEG400 as a plasticizer to decrease the glass temperature transition of PVA and increase the flexibility of the tape by breaking the close alignment and bonding of PVA chains.<sup>[11,14,14,27]</sup> PEG400 was used with a 1:1 plasticizer to binder ratio. Slurries were achieved by mixing the suspension with PVA and PEG400 in the planetary centrifugal mixer at 1000 rpm during 7 min and at 2000 rpm during 2 min and the excess of bubbles was outgassed in the machine during 2 min at 2000 rpm. As shown in Figure S3a, Supporting Information, the slurry including 10 wt% of PVA to solid loading leads to tape with cracks appearing during the drying process, indicating an insufficient amount of binder. Several tests performed by gradually increasing the amount of PVA (Figure S3b, Supporting Information) lead to determine that a minimum of 18 wt% of binder to solid loading is necessary to obtain a continuous polymer phase and a flexible tape with enough stiffness to be easily handled.

Despite the outgassing process, large bubbles were observed in the tape (Figure S3c, Supporting Information) and created porosity after a sintering treatment at 1600 °C during 2 h (Figure S3d, Supporting Information). To decrease the amount of bubbles with a better dispersion of ceramic particles, a surfactant was added. The mainly used surfactants in aqueous slurries are coco diethanolamide<sup>[12,20,25,26,28]</sup> and 2,4,7,9-tetramethyl-5-decyne-4,7-diol ethoxylate (TDDE)<sup>[15,27]</sup> but to avoid health toxicity of TDDE and for reasons of availability, polyethylene glycol sorbitan monolaurate (TWEEN20) was chosen. The coupling of NH4PAA and TWEEN20 surfactants combines electrostatic and steric repulsion mechanism, decreasing the amount of bubbles.<sup>[16,24]</sup> The weight percentage of TWEEN20 to solid loading was adjusted by testing its effect in a range from 0.3 to 2 wt% as selected based on reported results.<sup>[29]</sup> The amount of bubbles in green and sintered tapes is reduced whatever the selected amount of TWEEN20. Without a clear effect of an increase in the TWEEN20 content, to minimize the amount of additives, the 0.3 wt% TWEEN20 content is selected. The dissolution of PVA in water creates bubbles which could not be fully eliminated during the outgassing process, implying the use of an antifoam among which octanol is selected and its effect tested in a range from 2 to 10 wt% of antifoam to binder.<sup>[12,15,17,27,28,30]</sup> The optimal value allowing to obtain a bubble free tape after sintering is found to be equal to 5 wt% of antifoam to binder (Figure S3e,f, Supporting Information). However, it could be noticed that the addition of octanol induces slightly curled edges of the tapes after drying.

## 2.2. Slurries Preparation and Co-Tape-Casting

In addition to 8YSZ as electrolyte, NiO is selected as the oxide precursor of the anodic cermet with a composition 40 wt% of 8YSZ and 60 wt% of NiO. The SEM images (Figure S1c, Supporting Information) show that NiO is constituted of cubic grains with some sintering bridges and monomodal distribution with an average grain size of 194 nm (Figure S2c, Supporting Information). 10GDC is selected for the diffusion barrier layer. It has a spherical morphology (Figure S1b, Supporting Information) and a monomodal distribution with an average grain size of 91 nm (Figure S2b, Supporting Information).

The characterization of the influence of the nature and amount of the different additives on the behavior of the anode and DBL slurries (not detailed for reason of conciseness) shows that the composition already optimized for the electrolyte slurry can be transferred to the corresponding slurries. However, the loads of NiO/8YSZ and 10GDC have to be optimized to insure achieving porous anode and dense DBL.

The anode layer must be porous so the powder quantity in the slurry has to be reduced while a dense DBL is requested implying that the amount of powder should be maximized. The investigation of the effect of the amount of powder on the stability of the different slurries leads to define optimal composition of 45.8 wt % for NiO/8YSZ below which the viscosity of the slurry was too low and 49 wt% for 10GDC above which agglomerates starts to be formed. The optimized formulation of each of the different slurries is summarized in Table 1.

Figure 2 shows rheological characterization of the diffusion barrier layer, electrolyte, and anode slurries. The decrease of

**Table 1.** Formulation of the diffusion barrier layer, the electrolyte, and the anode slurries.

	DBL		Electrolyte		Anode	
	[wt%]	[vol%]	[wt%]	[vol%]	[wt%]	[vol%]
Powder 8YSZ	0	0.0	47.3	13.8	18.3	5.8
Powder NiO	0	0.0	0	0.0	27.5	8.1
Powder 10GDC	49.0	12.5	0	0.0	0	0.0
Solvent	32.1	55.1	34.0	57.7	35.6	56.2
Dispersant 1 (NH4PAA)	0.8	0.8	1.2	0.6	1.4	0.7
Binder	8.8	13.7	8.5	12.1	8.3	12.8
Plasticizer	8.8	14.4	8.5	12.7	8.3	13.5
Dispersant 2 (TWEEN20)	0.2	2.5	0.3	2.2	0.4	2.3
Antifoam	0.2	1.1	0.2	0.9	0.2	1.0

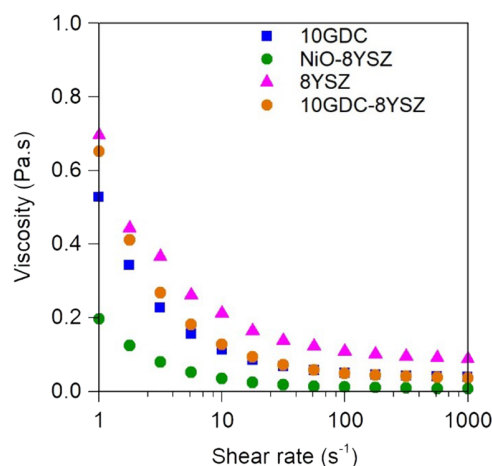


**Figure 2.** Variation of the viscosity as a function of shear rate of the diffusion barrier layer (10GDC), composite (10GDC-8YSZ), electrolyte (8YSZ), and anode (NiO-8YSZ) slurries.

the viscosity with the increase in shear rate shows that all slurries have a shear thinning behavior adequate for tape-casting as it allows an easy casting of the slurry which maintains shape and thickness during drying. At rest, anisotropic particles and long chains of molecules of additives create a high resistance against flow explaining the high viscosity of slurries. During casting, with increasing shear rates, all anisotropic particles and molecules are orienting toward the direction of the flow and agglomerates, if any, are split, which improve the fluidity and decrease the viscosity of slurries.<sup>[31,32]</sup> At high and low shear rate, the viscosity of DBL slurry was higher than the electrolyte one; itself higher than the anode slurry viscosity. At low shear rate, slurries viscosities are in the range of 0.2–0.7 Pa.s and decrease from 10 mPa s to 100 mPa s at high shear rate. This is in good correlation with the evolution of the solid content in the different slurries.<sup>[4,11]</sup>

The reverse sequential tape-casting process consists in casting first thinner layers, composed of 10GDC and 8YSZ slurries with a gap, respectively, of 30 and 40 μm. Thanks to the small thicknesses of the first layers and consequently a fast evaporation of water at ambient air, the anodic layer precursor can be quickly



cast with a 1200  $\mu\text{m}$  gap. The multilayer tape was dried during 10 h at ambient air leading to 60% reduction of the thickness mainly due to the elimination of the water and obtaining of 500  $\mu\text{m}$ -thick dried multilayer.

## 2.3. Cosintering, Warpage, and Interfaces Control

### 2.3.1. Organic Decomposition Thermal Profile

During the heat treatment, all organics must be removed and above all, the pores must be eliminated in the electrolyte part to obtain a dense layer. To determine the decomposition behavior of organic components, tapes have been first dried for 10 h in ambient conditions to remove the solvent and analyzed using TGA experiment. The TGA curve (Figure S4a, Supporting Information) shows, besides removal of remaining solvent at low temperature, two mass losses at 290 and 410  $^{\circ}\text{C}$  allowing to define the thermal profile (Figure S4b, Supporting Information) used for the sintering of the tape enlisting slow heating rate and intermediate dwells below 410  $^{\circ}\text{C}$  prior to reaching the sintering temperature.

### 2.3.2. Anodic Half-Cell without Composite Layer

Figure 3 shows the SEM image of the cross section of an anodic half-cell treated following the thermal profile described in Figure S4b, Supporting Information, with a sintering temperature of 1450  $^{\circ}\text{C}$  maintained during 2 h. The examination of the SEM image shows a very low amount of close porosity, indicating a dense and gas tight electrolyte layer with a thickness of 20  $\mu\text{m}$ . However, the delamination between the electrolyte and the DBL layer is also observed making the cell unusable because of the generated ohmic resistance. Snowdon et al. explained that a composite layer composed of the electrolyte and DBL materials is needed at the interface to avoid any delamination during the cosintering treatment.<sup>[14]</sup> The difference of thermomechanical

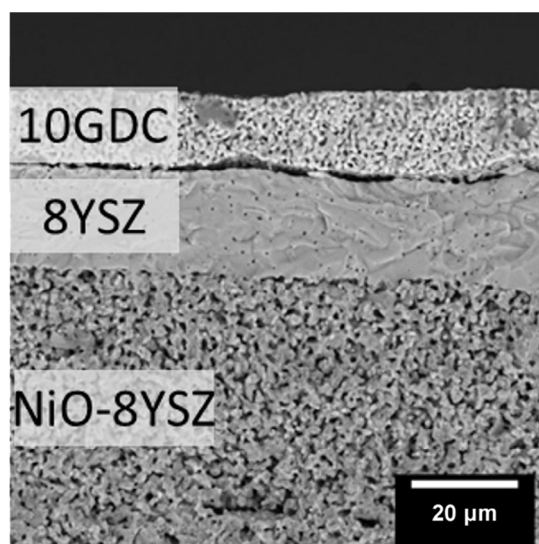


**Figure 3.** SEM image in BSE of the cross section of the anodic half-cell sintered at 1450  $^{\circ}\text{C}$  without composite layer.

behavior of the two materials and particularly the difference between their thermal expansion coefficients ( $3.12 \times 10^{-6} \text{ K}^{-1}$ ) explains the mechanical stress induced during thermal treatment sometimes leading to delamination.

### 2.3.3. Anodic Half-Cell with 10GDC-8YSZ Composite Layer

A composite slurry composed of 50 wt% of 8YSZ and 10GDC was then formulated by using the same organic ratio than the DBL slurry as summarized in Table 1. This 10GDC-8YSZ slurry exhibits a shear-thinning behavior and a viscosity matching the characteristics of the other slurries (0.65 Pa s at a low shear rate ( $1 \text{ s}^{-1}$ ) and 50 mPa s at high shear rate ( $1000 \text{ s}^{-1}$ )), as illustrated in Figure 2.

The reverse sequential tape-casting is then adapted to include this extra composite intermediate layer and the layers are casted as thin as possible. The 10GDC slurry is first casted with a 5  $\mu\text{m}$  gap followed by the 10GDC-8YSZ slurry with a 10  $\mu\text{m}$  gap, next the 8YSZ slurry with a 40  $\mu\text{m}$  gap, and finally the 8YSZ-NiO slurry is casted with a 2400  $\mu\text{m}$  gap. One has to note that while these gaps are adapted to reach targeted thickness of the sintered layers, the achieved thicknesses above requested ones for application are limited by the equipment used in this study. After drying, a flexible tape was obtained (Figure S5a, Supporting Information) and punched to obtain disks with 20 mm diameter and a total thickness of 1050  $\mu\text{m}$  (indicating a decrease of 55% during the drying process). As shown in the SEM image in Figure S5b, Supporting Information, the green tape exhibits neither delamination, cracks nor trapped bubbles. The electrolyte (Figure S5c, Supporting Information) and anodic (Figure S5d, Supporting Information) layers exhibit porosity and all oxide particles are coated by the binder and plasticizer, forming the 3D polymer network linked to the observed tapes flexibility.

### 2.3.4. Electrolyte Density and Cell Flatness Optimization

For stack assembly, cells must be flat but the mismatch of thermal expansion coefficients of individual layers leads to mechanical stresses and warping of the cell during the cosintering process (Figure S6, Supporting Information). The cell flatness and densification were controlled by using homemade (see Supporting Information) porous zirconia loads applied on samples during the thermal treatment. The use of loads helps maintain sample flatness without preventing shrinkage due to densification. Loads of different mass were prepared to apply a pressure in a range from 1.6 to 3.8  $\text{g cm}^{-2}$ . As observed in Figure S6, Supporting Information, cracks appear in the sample prepared using a 2.3  $\text{g cm}^{-2}$  load while the samples obtained using 2.7 and 3.8  $\text{g cm}^{-2}$  loads were both split into two pieces. The experiment with a 1.6  $\text{g cm}^{-2}$  load is the only one driving to an intact and deformation free sample so that this load is selected to produce planar half cells.

SEM images of the cross section and the surface of the optimized anodic half-cells cosintered at 1450 or 1500  $^{\circ}\text{C}$  during 2 h are presented in Figure 4. In both samples, the composite layer fulfilled its intended purpose of decreasing the risk of delamination between the electrolyte and DBL layers. A dense electrolyte of 20  $\mu\text{m}$  thick is obtained for both treatment temperatures. The difference was the thickness and the microstructure of the DBL

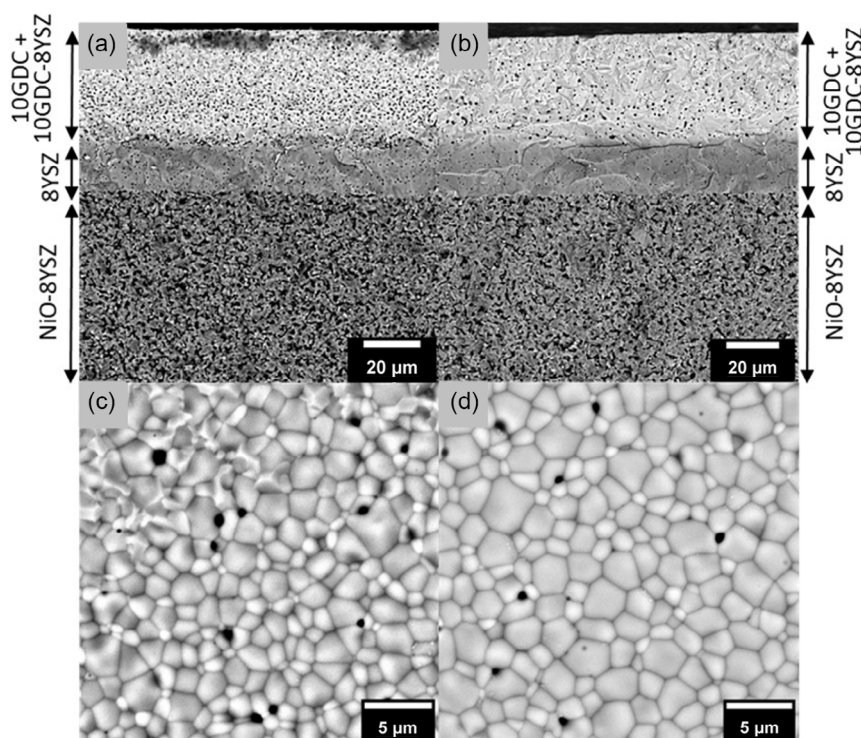


**Figure 4.** SEM images in BSE of the a) cross section and c) surface of the sample cosintered at 1450 °C 2 h, and the b) cross section and d) surface of the sample cosintered at 1500 °C 2 h.

layer: the higher the cosintering temperature, the denser is the DBL layer, avoiding porosity and consequently decreasing ohmic resistance. The average grain size, calculated by the intercept method, was about  $1.51 \pm 0.04 \mu\text{m}$  in the sample cosintered at 1450 °C during 2 h and  $1.94 \pm 0.06 \mu\text{m}$  in the sample cosintered at 1500 °C during 2 h, resulting in an increase of 29% of diameter size. A cosintering treatment of 1500 °C during 2 h would then be preferred to minimize the ohmic resistance by decreasing grain boundaries volume and closed porosity. With both cosintering temperature, the NiO-8YSZ layer was 530  $\mu\text{m}$  thick, a decrease of 78% from the green tape, reflecting the loss of organics and layers shrinkage. The shrinkage is then anisotropic (radial shrinkage of 20%).

### 2.3.5. Composition Profile and Structural Analysis

An energy-dispersive X-ray spectroscopy (EDS) analysis was performed in the cross section of the sintered anodic half-cell from the diffusion barrier layer to the anode (Figure S7, Supporting Information). A gradual composition is observed and there is no diffusion of NiO in the electrolyte layers. This analysis does not show interdiffusion, notably the absence of  $(\text{Zr}, \text{Ce})\text{O}_{2-x}$  solid solution with low ionic conductivity reported to be frequently observed during sintering above 1200 °C.<sup>[33–37]</sup> The DBL and anode surface of anodic half-cells sintered at 1500 °C during 2 h are analyzed by XRD (Figure 5a,b). On the DBL side, the  $\text{Ce}_{0.9}\text{Gd}_{0.1}\text{O}_{1.95}$  cubic phase (PDF: 01-075-0161) is indexed without any secondary phase. On the anodic side, the cubic phase  $\text{Zr}_{0.84}\text{Y}_{0.16}\text{O}_{2-\delta}$  (PDF: 00-030-1468) and the NiO cubic phase (PDF: 03-065-2901) are also indexed without any secondary phase.

The behavior of the oxide precursor during the selective reduction of NiO to obtain the Ni-8YSZ anode is investigated by annealing the half cell at 750 °C during 30 min under  $100 \text{ mL min}^{-1}$  of  $\text{H}_2$ . As shown in Figure 5c, 8YSZ is intact and all the NiO is reduced down to the metal state. One has to note that despite a loss of oxygen, both cohesiveness and size of the half-cell are maintained during the reduction step.

### 2.3.6. Cathode Deposition—Complete Cell

The cathode is deposited using widely used process without further optimization.<sup>[38]</sup>  $\text{La}_2\text{NiO}_{4+\delta}$  is selected as the cathode material. The investigation on the LNO powder using SEM (Figure S1d and S2d, Supporting Information) shows the presence of some sintering bridges between particles with an average size of 276 nm. An ink vehicle was prepared by dissolving 6 wt% of ethyl cellulose in 94 wt% of terpineol at 60 °C during 30 min under stirring. Then, the  $\text{La}_2\text{NiO}_{4+\delta}$  powder was added to the ink vehicle to obtain a solid loading of 60 wt% and mixed during 1 min at 2000 rpm. The cathode layer was then deposited by screen printing through a 325 mesh on an anodic half-cell prepared as described above (previously cosintered at 1500 °C during 2 h), dried at 40 °C during 1 h followed by a consolidation thermal treatment at 1150 °C during 2 h.

## 2.4. Electrochemical Testing

The behavior of the as-obtained all oxide precursor full SOFC is tested in a temperature and atmosphere controlled bench

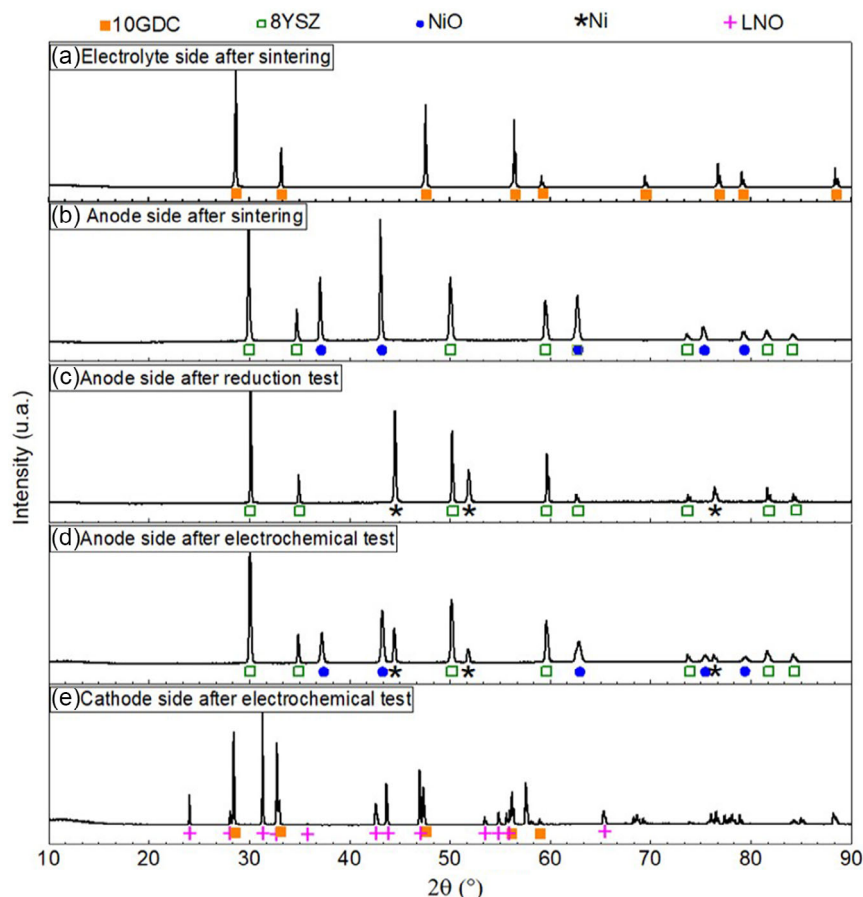


**Figure 5.** XRD patterns of a) the electrolyte side after the sintering treatment, b) the anode side after sintering, c) the reduction test and d) after the electrochemical test and e) of the cathode side after the electrochemical test.

(Fiixell). The cell with 16 mm diameter and 650  $\mu\text{m}$  thick is placed in the electrochemical setup with gold and nickel current collectors on the cathode and anode side, respectively. The cell is heated up to 730  $^{\circ}\text{C}$  with a 200  $^{\circ}\text{C h}^{-1}$  rate under  $\text{N}_2$  flow on the anode side. After temperature stabilization, gas flow of 400  $\text{mL min}^{-1}$  of air at the cathode side and 100  $\text{mL min}^{-1}$  of  $\text{H}_2$  at the anode side are used during the  $I/V$  measurement performed at 730, 780, and 830  $^{\circ}\text{C}$ . The evolution of the current–voltage ( $I-V$ ) reported in Figure 6 shows linear evolutions with decreasing slopes with increasing temperature in agreement with expected enhancement of the conductivity. In addition, the current–power density ( $I-P$ ) curves for button cells measured from the OCV (1.05 V) to 0.1 V shows that the power density increases until it reaches 145, 227, and 319  $\text{mW cm}^{-2}$  at 730, 780, and 830  $^{\circ}\text{C}$  respectively. These performances are in the range of reported ones for anode-supported Ni-YSZ SOFC considering the thicknesses of the barrier layer-composite-electrolyte used for the studied sample.<sup>[39]</sup>

Figure 5 shows the XRD patterns collected on the different parts of the cell after the electrochemical test. On the cathode side (Figure 5e), the tetragonal phase of  $\text{La}_2\text{NiO}_{4+\delta}$  (LNO, PDF 01-072-1241) and 10GDC was indexed without any other phase which demonstrates the efficiency of the as-integrated 10GDC diffusion barrier layer. On the anode side (Figure 5d), there is

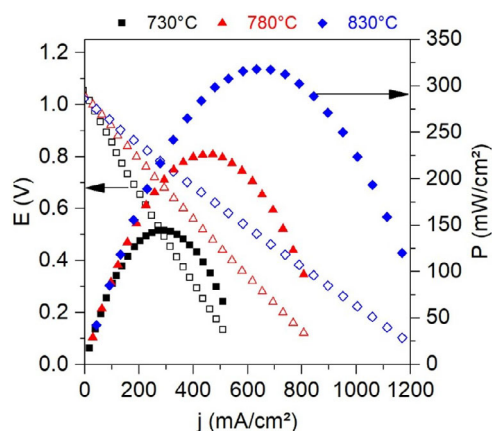


**Figure 6.**  $I-V$  and  $I-P$  curves at 730, 780, and 830  $^{\circ}\text{C}$ .

the presence of 8YSZ, a cubic phase of Ni, and remaining NiO, indicating that the reduction occurring during the warm-up is not complete.

Figure 7a shows the cross section of the cell after working cycle. All layers are intact without any delamination or cracking and all interfaces are well demarked, indicating the stability of



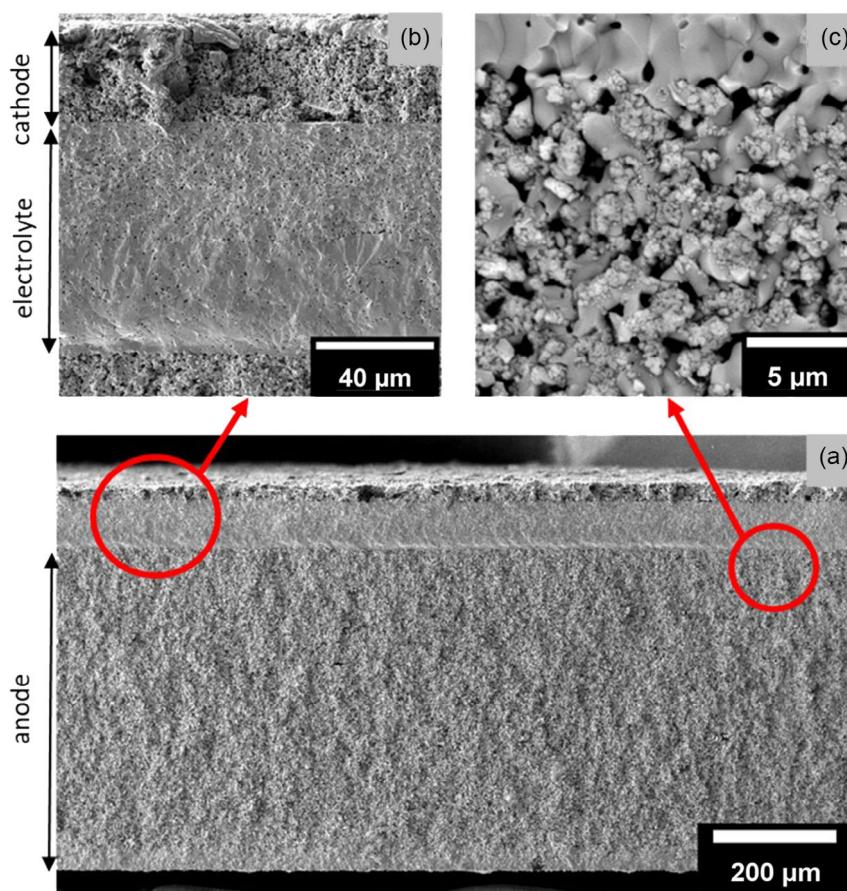


**Figure 7.** SEM image of the cross section of the cell after the electrochemical testing of c) the entire cell with secondary electrons, with a zoom on a) the cathode and electrolyte layer with secondary electrons and on b) the interface between the electrolyte and the anode with backscattered electrons.

the different layers and of their interfaces. Figure 7a,c shows a continuous and porous 30  $\mu\text{m}$ -thick cathode layer on a homogeneous 80  $\mu\text{m}$ -thick electrolyte (GDC, composite GDC-8YSZ and 8YSZ layers). The backscattered image of the electrolyte and anode interface (Figure 7b) shows two phases in a 530  $\mu\text{m}$ -thick porous anode layer containing agglomerates of Ni in an 8YSZ porous scaffold. Microstructures are typical for SOFC and comply with electrodes and electrolyte specifications.

Postmortem analyses confirm that the manufacturing of anodic half-cell including the barrier layer in only one heat treatment leads to obtain a cell with standard electrolyte and electrodes microstructures. While performances and stability of the cell have been assessed, it appears that NiO reduction was not complete and that despite adequate to the cell characteristics, performances can be improved by tuning the thickness of, in particular, the electrolyte layer. Both remaining issues are, respectively, related to size mismatch between the cell and electrochemical setup inducing bad sealing and possible leakage (inducing low OCV) and for the second point to the too low accuracy of the setup used for the tape-casting in this work which does not allow tuning the multilayer electrolyte thickness lower than 80  $\mu\text{m}$ .

Tape-casting being a widely used technique for industrial manufacturing, the process developed in this work can be easily scaled up to produce, e.g., 400  $\times$  400  $\text{mm}^2$  cells<sup>[40]</sup> and the

decrease of the barrier layer-composite-electrolyte layers thicknesses can be easily achieved by using a more accurate tape-casting equipment to approach the electrolyte thickness (10–15  $\mu\text{m}$ ) of the most performing SOFC cell.<sup>[40]</sup>

### 3. Conclusion

The optimization of the formulation of slurries allows to propose a low-cost and environmental-friendly manufacturing process of SOFC. While the cathode is deposited on top of the anodic half-cell using conventional screen-printing method, the anodic half-cell is obtained via a single cosintering process of a multilayer tape including anode, electrolyte, and diffusion barrier layer. To insure appropriate interfaces between 8YSZ electrolyte and 10GDC DBL, an intermediate 8YSZ-10GDC composite has been added. Four different layers with mastered microstructures and thicknesses have been successfully assembled by the use of reverse sequential tape-casting process and sintered in only one step. The four different slurries are based on aqueous solvent and includes besides adequate oxide materials, nontoxic additives. Their formulation has been optimized resulting in high stability and shear-thinning behavior suitable for tape-casting application. The control of the thermal treatment



parameters applied on the multilayer tape leads to master the thickness of the different layers, the planarity, and homogeneous adhesion at the interfaces as well as to adjust the relative density of each layer from fully dense for electrolyte and DBL to porous for the anode while preventing the presence of defects, delamination, or interdiffusion. The use of a load during the cosintering treatment of the anodic half-cell demonstrated its efficiency for flatness control. The characterization of the obtained SOFC in functioning conditions shows that besides remaining issues associated to the experimental setup used (leakage in the electrochemical setup and low accuracy of the tape-casting setup), the oxide precursor is selectively reduced during the warm-up while maintaining the integrity of all interfaces, leading to performances ( $319 \text{ mW cm}^{-2}$  at  $830^\circ\text{C}$ ) perfectly matching expected ones considering the electrolyte thickness. Knowing that the later can be easily optimized with adequate tape-casting equipment and that the cell size has to be adjusted to the setup, one can conclude that this optimized low cost and eco-friendly process based on techniques widely used at the industrial scale is a promising strategy to produce next generation of SOFC.

## 4. Experimental Section

**Methods:** 8 mol% yttria-stabilized zirconia 8YSZ (TZ-8, Tosoh) was used as the electrolyte and 10 mol% gadolinium-doped ceria 10GDC (Marion Technologies) was used as diffusion barrier layer. Nickel nitrate hexahydrate (CAS: 13478-00-7, Sigma-Aldrich) was dissolved in deionized water and the solution was progressively heated in air up to  $800^\circ\text{C}$  maintained during 2 h to synthesize NiO.  $\text{La}_2\text{NiO}_{4+\delta}$  powders were prepared using a Pechini route<sup>[41]</sup> in which lanthanum nitrate  $\text{La}(\text{NO}_3)_3 \cdot 6\text{H}_2\text{O}$  (CAS: 10277-43-7, Sigma-Aldrich) and nickel nitrate  $\text{Ni}(\text{NO}_3)_2 \cdot 6\text{H}_2\text{O}$  (CAS: 13478-00-7, Sigma-Aldrich) were used as cationic precursors salts. Stoichiometric amount of metallic salts were dissolved in DI water. A liquid polymeric matrix, composed of hexamethylenetetramine, acetylacetone (in equimolar ratio), and acetic acid, was then added. The polyesterification and polycondensation reactions were activated with a thermal treatment at  $90^\circ\text{C}$  during 20 min. A decomposition treatment at  $400^\circ\text{C}$  during 7 h in air eliminated organic compounds and the crystallized oxide was obtained with a final thermal treatment at  $900$  or  $1000^\circ\text{C}$  during 2 h. This final annealing temperature was selected to control the crystallite size of the powder in order to obtain a specific surface allowing an easy dispersion in the solvent while permitting a further consolidation treatment of the layer.

The binder solution used in slurries was prepared by dissolving 30 wt% of PVA (CAS: 9002-89-5, Sigma-Aldrich) in water at  $80^\circ\text{C}$  during 30 min. Ammonium polymethacrylate NH4PAA (CAS: 30875-88-8, Vanderbilt Chemicals) and TWEEN20 (CAS: 9005-64-05, Polyethylene glycol sorbitan monolaurate, TWEEN 20, Sigma Aldrich) were used as dispersants, PEG400 (CAS: 25322-68-3, poly(ethylene glycol), Sigma-Aldrich) as plasticizer, and octanol (CAS: 111-87-5, 1-Octanol, Sigma-Aldrich) as antifoam.

The screen-printing ink vehicle contained ethyl cellulose as a binder (CAS: 9004-57-3, Sigma-Aldrich) and terpineol as a solvent (CAS: 98-55-5, Sigma-Aldrich).

An ultrasonic bath (Bandelin) was used to deagglomerate oxide particles in suspensions. Slurries and inks were prepared by using a planetary centrifugal mixer (SK-300SII, Kakuhunter) for its mixing and outgassing functions.

An automatic film applicator (AB3655, TQC Sheen) and a micrometer adjustable doctor blade were used to apply slurries. The bar spread the slurry at a chosen constant speed of  $10 \text{ mm s}^{-1}$  on a  $75 \mu\text{m}$ -thick silicone-coated polyester sheet (PET SRF 121, HiFi Industrial Film) fixed on the automatic film applicator.

**Characterization:** The rheological behavior of slurries was characterized through a rheometer from 1 to  $1000 \text{ s}^{-1}$  shear rate (Physica MCR 301,

Anton Paar) with parallel discs and a 25 mm diameter module. The organics elimination temperature was determined with thermogravimetric analysis (Setaram TG DTA 92) by heating in air dried tapes from  $20$  to  $800^\circ\text{C}$  with a  $1^\circ\text{C min}^{-1}$  heating rate. The dried tapes were cut in discs and the optimum cosintering temperature was then determined. XRD was performed using a BRUKER D8 Endeavor diffractometer operating in Bragg-Brentano mode with a Cu K $\alpha$  X-ray source with wavelength of  $\lambda_{\text{K}\alpha 1} = 1.5406 \text{ \AA}$  and  $\lambda_{\text{K}\alpha 2} = 1.544 \text{ \AA}$ . All scans were collected in the  $2\theta$  range  $10^\circ$ – $100^\circ$  with an angular step  $2\theta = 0.0157^\circ$ . The electrical characterization was performed with a FIAXELL bench test<sup>[42]</sup> on button cells with a 16 mm diameter half-cell and an effective area of  $0.79 \text{ cm}^2$ . A gold grid on the cathode side and a nickel foam on the anode side were used as current collectors. Electrochemical performances were measured (with IVIUM Technology) with  $400 \text{ mL min}^{-1}$  of air as oxidant on the cathode side and  $100 \text{ mL min}^{-1}$  dry  $\text{H}_2$  as fuel on the anode side. The sealing of the cell was obtained by the pressure differential of the  $\text{O}_2$  and  $\text{H}_2$  flow. The cell was heated under  $\text{N}_2$  flow on the anode side with a  $200^\circ\text{C h}^{-1}$  rate until it reached the testing temperature. After 30 min of temperature stabilization, the  $\text{N}_2$  flow was progressively substituted by the  $\text{H}_2$  fuel gaz. The  $I/V$  measurement was then performed after 30 min to obtain the cermet anode. SEM was used to observe powders with carbon metallization using with JSM-7800F and the surface and cross-sectional microstructure of the cells with Au/Pd metallization using Tescan Vega3. EDX measurements were performed to characterize the elemental distribution throughout the thickness of cells.

## Supporting Information

Supporting Information is available from the Wiley Online Library or from the author.

## Acknowledgements

This work was carried out on the hydrogen platform of Toulouse developed as part of the PACAERO project and funded by the European Union (FEDER), the French state, the Occitanie region and Toulouse metropolis (CPER).

## Conflict of Interest

The authors declare no conflict of interest.

## Data Availability Statement

The data that support the findings of this study are available from the corresponding author upon reasonable request.

## Keywords

aqueous processing, ceramic processes, cosintering, sequential tape-casting, solid oxide fuel cells (SOFCs)

Received: January 9, 2023

Revised: May 10, 2023

Published online: August 8, 2023

[1] M. Singh, D. Zappa, E. Comini, *Int. J. Hydrogen Energy* **2021**, *46*, 27643.

[2] A. Montenegro-Hernández, J. Vega-Castillo, L. Moggi, A. Caneiro, *Int. J. Hydrogen Energy* **2011**, *36*, 15704.

- [3] A. M. Hernández, L. Mogni, A. Caneiro, *Int. J. Hydrogen Energy* **2010**, 35, 6031.
- [4] H. Moon, S. D. Kim, S. H. Hyun, H. S. Kim, *Int. J. Hydrogen Energy* **2008**, 33, 2826.
- [5] J. Myung, H. J. Ko, C. H. Im, J. Moon, S.-H. Hyun, *Int. J. Hydrogen Energy* **2014**, 39, 2313.
- [6] C. Jia, M. Chen, M. Han, *Int. J. Appl. Ceram. Technol.* **2017**, 14, 1006.
- [7] X. Chen, W. Ni, X. Du, Z. Sun, T. Zhu, Q. Zhong, M. Han, *J. Mater. Sci. Technol.* **2019**, 35, 695.
- [8] R. Wang, C. Byrne, M. C. Tucker, *Solid State Ionics* **2019**, 332, 25.
- [9] M. Cologna, V. M. Sglavo, M. Bertoldi, *Int. J. Appl. Ceram. Technol.* **2010**, 7, 703.
- [10] M. Liu, Y. Liu, *Int. J. Hydrogen Energy* **2019**, 44, 8103.
- [11] S. Ramanathan, K. P. Krishnakumar, P. K. De, S. Banerjee, *J. Mater. Sci.* **2004**, 39, 3339.
- [12] C. Fu, S. H. Chan, Q. Liu, X. Ge, G. Pasciak, *Int. J. Hydrogen Energy* **2010**, 35, 11200.
- [13] N. A. Arifin, *Degree Thesis*, University of Birmingham, **2018**.
- [14] A. L. Snowdon, Z. Jiang, R. Steinberger-Wilckens, *Int. J. Appl. Ceram. Technol.* **2022**, 19, 289.
- [15] J. Zhou, Q. Liu, Q. Sun, S. Hwa Chan, *Fuel Cells* **2014**, 14, 667.
- [16] Q. Tan, Z. Zhang, Z. Tang, S. Luo, K. Fang, *Mater. Lett.* **2003**, 57, 2375.
- [17] C. Goulart, D. de Souza, *Int. J. Appl. Ceram. Technol.* **2017**, 14, 413.
- [18] M. P. Albano, L. B. Garrido, *Mater. Sci. Eng., A* **2006**, 420, 171.
- [19] T. Chartier, A. Bruneau, *J. Eur. Ceram. Soc.* **1993**, 12, 243.
- [20] J. Aguilar-Arias, D. Hotza, P. Lenormand, F. Ansart, *J. Am. Ceram. Soc.* **2013**, 96, 3075.
- [21] F. Snijders, A. de Wilde, S. Mullens, J. Luyten, *J. Eur. Ceram. Soc.* **2004**, 24, 1107.
- [22] T. Baquero, J. Escobar, J. Frade, D. Hotza, *Ceram. Int.* **2013**, 39, 8279.
- [23] R. Krishnan P. P., S. Vijayan, P. Wilson, P. Arun Kumar, K. Prabhakaran, *Ceram. Int.* **2019**, 45, 18543.
- [24] D. Hotza, P. Greil, *Mater. Sci. Eng., A* **1995**, 202, 206.
- [25] M. dos Reis Araújo, W. Acchar, *Mater. Today Proc.* **2017**, 4, 11506.
- [26] D. M. Amaya, D. Estrada, D. Hotza, J. B. Rodrigues Neto, J. A. Escobar, *J. Eur. Ceram. Soc.* **2017**, 37, 5233.
- [27] J. Zhou, L. Zhang, C. Liu, J. Pu, Q. Liu, C. Zhang, S. H. Chan, *Int. J. Hydrogen Energy* **2019**, 44, 21110.
- [28] A. Akbari-Fakhrabadi, R. V. Mangalaraja, F. A. Sanhueza, R. E. Avila, S. Ananthakumar, S. H. Chan, *J. Power Sources* **2012**, 218, 307.
- [29] B. J. Palla, D. O. Shah, *J. Colloid Interface Sci.* **2000**, 223, 102.
- [30] D. A. Knowles, *Chemistry and Technology of Agrochemical Formulation*, Springer Netherlands, Dordrecht, Netherlands **1998**.
- [31] M. Jabbari, R. Bulatova, A. I. Y. Tok, C. R. H. Bahl, E. Mitsoulis, J. H. Hattel, *Mater. Sci. Eng., B* **2016**, 212, 39.
- [32] G. Schramm, *A Practical Approach to Rheology and Rheometry*, Thermo Haake, Karlsruhe, Germany **1998**.
- [33] A. Tsoga, A. Gupta, A. Naoumidis, D. Skarmoutsos, P. Nikolopoulos, *Ionics* **1998**, 4, 234.
- [34] A. Tsoga, A. Naoumidis, A. Gupta, D. Stöver, *MSF* **1999**, 308–311, 794.
- [35] B. Liang, T. Tao, S. Zhang, Y. Huang, Z. Cai, S. Lu, *J. Alloys Compd.* **2016**, 679, 191.
- [36] T. Kawada, H. Yokokawa, M. Dokiya, N. Sakai, T. Horita, J. Van Herle, K. Sasaki, *J. Electroceram.* **1997**, 1, 155.
- [37] A. Mahmood, S. Bano, J. H. Yu, K.-H. Lee, *Energy* **2015**, 90, 344.
- [38] Y. Zhang, X. Huang, Z. Lu, X. Ge, J. Xu, X. Xin, X. Sha, W. Su, *Solid State Ionics* **2006**, 177, 281.
- [39] D. Udomsilp, C. Lenser, O. Guillon, N. Menzler, *Energy Technol.* **2021**, 9, 2001069.
- [40] N. H. Menzler, F. Tietz, S. Uhlenbruck, H. P. Buchkremer, D. Stöver, *J. Mater. Sci.* **2010**, 45, 3109.
- [41] M. L. Fontaine, C. Laberty-Robert, M. Verelst, J. Pielaszeck, P. Lenormand, F. Ansart, P. Tailhades, *Mater. Res. Bull.* **2006**, 41, 1747.
- [42] Fiixell SOFC Technologies, Fiixell, <https://fiixell.com/> (accessed: December 2022).